

# Nucleon structure and high energy interactions

O.V. Selyugin<sup>\*1</sup>

<sup>1</sup>*Bogoliubov Laboratory of Theoretical Physics,  
Joint Institute for Nuclear Research, 141980 Dubna, Moscow region, Russia*

On the basis of the representation of the generalized structure of nucleons a new model of the hadron interaction at high energies is presented. The new  $t$ -dependence of the generalized parton distributions (GPDs) is obtained from the comparative analysis of different sets of the parton distribution functions (PDFs), based on the description of the whole sets of experimental data of electromagnetic form factors of the proton and neutron. Taking into account the different moments of GPDs of the hadron the quantitative descriptions of all existing experimental data of the proton-proton and proton-antiproton elastic scattering from  $\sqrt{s} = 9.8$  GeV to 8 TeV, including the Coulomb range and large momentum transfers up to  $-t = 15$  GeV<sup>2</sup>, are obtained with a few free fitting high energy parameters. The real part of the hadronic elastic scattering amplitude is determined only through complex  $s$  satisfying the dispersion relations. The negligible contributions of the hard Pomeron and the presence of the non-small contributions of the maximal Odderon are obtained. The non-dying form of the spin-flip amplitude is examined as well. The structure of the Born term and unitarized scattering amplitude are analysed. It is shown that the Black Disk Limit for the elastic scattering amplitude is not reached at LHC energies. Predictions for LHC energies are made.

PACS numbers: 13.40.Gp, 14.20.Dh, 12.38.Lg

## I. INTRODUCTION

A topical problem of modern physics of elementary particles, the exploring of the dynamics of the strong interaction processes at high energies, is considered in the framework of different approaches using various models of the structure of hadrons and the dynamics of their interactions. Different models for the description of hadron interaction at large distances are developed. They are based on the general quantum field theory principles (analyticity, unitarity, and so on). The relativistic models of high energy scattering based on the quasipotential approach [1, 2] occupy an important place among them. Here, the hypothesis about the existence of the local smooth quasipotential giving an adequate description of high energy scattering processes is essential. In the region of small angles of the scattering the eikonal approach can be used as a consequence of the smoothness of the quasipotential [3]. The smoothness of the quasipotential is related to the dynamics of two-particle interactions and means that at high energies the hadrons behave as loose extended objects with finite dimensions.

The elastic hadron-hadron scattering plays an important role in the investigation of the strong interaction. For the description of the interaction at small distances there is the exact theory, QCD, but for the interaction at large distances, which is the basis for the elastic scattering at small angles, the calculation in the framework of QCD is impossible at present. These two domains are tightly connected

with the experimental determination of the parameters of the elastic scattering and are very important for the development of the modern strong interaction theory [4].

Only in the region of small angles the basic properties of the non-perturbative strong interaction: the total cross section, the slope of the diffraction peak and the parameter  $\rho(s, t)$  - ratio of the real part to the imaginary part of the scattering amplitude, can be measured. Their values are connected, on the one hand, with the large-scale structure of hadrons and, on the other hand, with the first principles which lead to the theorems on the behavior of the scattering amplitudes at asymptotic energies [5, 6].

There are indeed many different models for the description of hadron elastic scattering at small angles [7, 8]. They lead to the different predictions for the structure of the scattering amplitude at asymptotic energies, where the diffraction processes can display complicated features [9]. This concerns especially the asymptotic unitarity bound connected with the Black Disk Limit (BDL) [10] and the influence of the saturation regime on the differential cross sections [11].

In the Chow-Yang model [12, 13] it was assumed that the hadron interaction is proportional to the overlapping of the matter distribution of the hadrons, and Wu and Yang [12] suggested that the matter distribution is proportional to the charge distribution of the hadron. Many models used the electromagnetic form factors of the hadron but, in most part, they changed its form to describe the experimental data, as was made in the famous Bourrely-Soffer-Wu model [14]. The parameters of the obtained form-factor are determined by the fit of the differential cross sections. The authors noted that

---

<sup>\*</sup>selugin@theor.jinr.ru

the form factor is "parameterized like an electromagnetic form factor, as two poles, and the slowly varying function reflects the approximate proportionality between the charge density and hadronic matter distribution inside a proton."

In paper [15], it was proposed that the hadron form factor is proportional to the matter distribution. The matter distributions in the hadron are tightly connected with the energy momentum tensor [16]. In [17], it was noted that "the gravitational form factors are related to the matrix elements of the energy-momentum tensor in a hadronic state, thus providing the distribution of matter within the hadron". The recent picture of the hadron structure is determined by the general parton distributions (GPDs) [18, 19] which include as part the parton distribution functions (PDFs). The first and second moments of GPDs give two hadron form factors.

Before the introduction of GPDs a similar representation for the scattering amplitude was used in work of S. Sanielevici and P. Valin (1984) [20]

$$K_p(q^2) = \frac{1}{3} \int_0^1 dx \, x [2L_p^U(x) T_p^U(\vec{k}) + 2L_p^D(x) T_p^D(\vec{k})];$$

Here the function  $L_p^{U,D}(x)$  represents the parton distributions and  $T_p^{U,D}(\vec{k})$  represents the transfer momentum dependence. Note that the whole structure of the amplitude corresponds to the second moment of GPDs.

Usually, models of high energy hadron interaction include a different kind of leading Reggions: one or a few pomerons (including the soft and hard pomerons), the odderons with intercept equal to the pomeron (maximal odderon) or with intercept close (or less) unity and sometimes the spin-flip amplitude. The effect of the hard pomeron contribution on the elastic differential cross sections is very important for understanding the properties of QCD in the non-perturbative regime [21]. Note that  $\rho(s, t)$  of the hard pomeron is essentially larger than  $\rho(s, t)$  of the soft pomeron. In [22], it is suggested that such a contribution can explain the preliminary result of the TOTEM Collaboration [23] on the elastic proton-proton differential cross sections.

In our high energy general structure (HEGS) model [24], the real part of the hadronic amplitude is determined only through complex  $s$  satisfying the cross symmetric relation. In the framework of the model, the quantitative description of all existing experimental data at  $52.8 \leq \sqrt{s} \leq 1960$  GeV, including the Coulomb range and large momentum transfers  $0.0008 \leq |t| \leq 9.75$  GeV<sup>2</sup>, is obtained with only 3 fitting high energy parameters. The comparison of the predictions of the model at 7 TeV and preliminary data of the TOTEM collaboration are shown to coincide well. In [25], the contribution of the hard pomeron in the elastic scattering at small angles at high energies was examined. It was found

that such a contribution is invisible in the existing experimental data including the new data of LHC. In [26], they came to the same result.

In the framework of the model, only the Born term of the scattering amplitude is introduced. Then the whole scattering amplitude is obtained as a result of the unitarization procedure of the hadron Born term that is then summed with the Coulomb term. The Coulomb-hadron interference phase is also taken into account. The essential moment of the model is that both parts of the Born term of the scattering amplitude have the positive sign, and the diffraction structure is determined by the unitarization procedure.

Now we present the extended variant of the HEGS model [24], based on the assumption that the hadron interaction is sensitive to the generalized parton distributions (GPDs), whose moments can be represented in the form of two different distributions: charge and matter, separately. Hence, this model used the exact electromagnetic and matter form-factors determined by one function - generalized parton distributions (GPDs). Both the form factors are independent of the fitting procedure of the differential cross sections of the elastic hadron scattering. Note that the form of GPDs is determined, on the one hand, by the deep-inelastic processes and, on the other hand, by the measure of the electromagnetic form factor from the electron-nucleon elastic scattering. We support this picture by a good description of the experimental data in the Coulomb-hadron interference region and large momentum transfer at high energies by one amplitude with a few free parameters.

The differential cross sections of nucleon-nucleon elastic scattering can be written as the sum of different helicity amplitudes:

$$\frac{d\sigma}{dt} = \frac{2\pi}{s^2} (|\Phi_1|^2 + |\Phi_2|^2 + |\Phi_3|^2 + |\Phi_4|^2 + 4|\Phi_5|^2). \quad (1)$$

The total helicity amplitudes can be written as  $\Phi_i(s, t) = F_i^h(s, t) + F_i^{\text{em}}(s, t)e^{\varphi(s, t)}$ , where  $F_i^h(s, t)$  comes from the strong interactions,  $F_i^{\text{em}}(s, t)$  from the electromagnetic interactions and  $\varphi(s, t)$  is the interference phase factor between the electromagnetic and strong interactions [27–29].

The structure of the paper is as follows: first, in Section 2 the basis of the first variant of the HEGS model is discussed shortly.

In Section 3, the hadron form factors are analyzed by the new form of the general parton distributions (GPDs) with taking into account two forms of PDFs, which give the best descriptions of the electromagnetic form factors of the proton and neutron. As a result, the new forms of the electromagnetic and matter form factors are obtained.

Section 4 is devoted to the study of all existing experimental data of the proton-proton and proton-antiproton elastic scattering from  $\sqrt{s} = 9.8$  GeV

to 8 TeV, including the Coulomb range and large momentum transfers up to  $-t = 15 \text{ GeV}^2$  in the framework of the model with a few free fitting high energy parameters.

In section 5, the structure of the elastic hadron scattering amplitude, obtained in the framework of the model, is analyzed. First, the Born term of the scattering amplitude is discussed with its cross-even and cross-odd separate parts. Then the obtained overlapping function is considered in the impact parameter representation. And, finally, the full form of the scattering amplitude, obtained after integration over the impact parameter, is considered. Especially, we examine the energy and momentum transfer dependence of the slope of the scattering amplitude as the Born term and as the full term of the scattering amplitude. Finally, the obtained results and the comparison with other models and some predictions of our model are discussed in Section 6.

## II. THE HIGH ENERGY GENERAL STRUCTURE (HEGS) MODEL

The model is based on the representation that at high energies the hadron interaction in the non-perturbative regime is determined by the reggenized-gluon exchange. The cross-even part of this amplitude can have two non-perturbative parts, possible standard pomeron -  $P_{2g}$  and the cross-even part of three non-perturbative gluons  $P_{3g}$ . The interaction of these two objects is proportional to two different form factors of the hadron. This is the main assumption of the model. Of course, we cannot insist on the origin of the second term of the scattering amplitude. However, in any case, it has the cross-even properties, positive sign and the slope is the same as for the odderon. The second important assumption is that we chose the slope of the second term four times smaller than the slope of the first term. All terms have the same intercept.

The form factors are determined by the general parton distributions of the hadron (GPDs) [30]. The first form factor, corresponding to the first momentum of GPDs is the standard electromagnetic form factor -  $G(t)$ . The second form factor is determined by the second momentum of GPDs -  $A(t)$ . The parameters and  $t$ -dependence of the GPDs are determined by the standard parton distribution functions, so by the experimental data on the deep inelastic scattering and by the experimental data for the electromagnetic form factors (see [31]).

The electromagnetic form factors can be represented as the first moments of GPDs with  $\xi = 0$

$$F_1(t) = \int_0^1 dx \sum_{u,d} \mathcal{H}^q(x,t); \quad (2)$$

$$F_2(t) = \int_0^1 dx \sum_{u,d} \mathcal{E}^q(x,t),$$

In [31] the  $t$ -dependence of GPDs in the form

$$\begin{aligned} \mathcal{H}^q(x,t) &= q(x)_{nf} \exp[a_+ \frac{(1-x)^2}{x^m} t]; \\ \mathcal{E}^q(x,t) &= q(x)_{sf} \exp[a_- \frac{(1-x)^2}{x^m} t]; \end{aligned} \quad (3)$$

was researched. The function  $q(x)$  was chosen at the same scale  $\mu^2 = 1$  as in [32], which is based on the MRST2002 global fit [33].

For  $\xi = 0$  one has the second moment of GPDs

$$\int_0^1 dx x \sum_{u,d} [\mathcal{H}(x,t) \pm \mathcal{E}(x,t)] = A_h(t) \pm B_h(t). \quad (4)$$

The integration of the second moment of GPDs over  $x$  give the momentum-transfer representation of the form factor. It was approximated by the dipole form [24]  $A(t) = L_2^4 / (L_2^2 - t)^2$ .

Hence, the Born term of the elastic hadron amplitude can be written as

$$\begin{aligned} F_h^{Born}(s,t) &= h_1 G^2(t) F_a(s,t) (1 + r_1/\hat{s}^{0.5}) \\ &+ h_2 A^2(t) F_b(s,t) (1 + r_2/\hat{s}^{0.5}), \end{aligned} \quad (5)$$

where  $F_a(s,t)$  and  $F_b(s,t)$  have the standard Regge form

$$F_a(s,t) = \hat{s}^{\epsilon_1} e^{B(s)t}, \quad F_b(s,t) = \hat{s}^{\epsilon_1} e^{B(s)/4 t}. \quad (6)$$

The slope of the scattering amplitude has the logarithmic dependence on the energy,  $B(s) = \alpha' \ln(\hat{s})$ , with  $\alpha' = 0.24 \text{ GeV}^{-2}$  and  $\hat{s} = s e^{-i\pi/2}/s_0$ ,  $s_0 = 1 \text{ GeV}^2$ . The final elastic hadron scattering amplitude is obtained after unitarization of the Born term. So, first, we have to calculate the eikonal phase

$$\chi(s,b) = -\frac{1}{2\pi} \int d^2q e^{i\vec{b}\cdot\vec{q}} F_h^{Born}(s,q^2) \quad (7)$$

and then obtain the final hadron scattering amplitude

$$F_h(s,t) = is \int b J_0(bq) \Gamma(s,b) db \quad (8)$$

with

$$\Gamma(s,b) = 1 - \exp[\chi(s,b)]. \quad (9)$$

The model has only three high-energy fitting parameters and two low-energy parameters, which reflect some small contribution coming from the different low-energy terms.

We take all existing experimental data in the energy range  $52.8 \leq \sqrt{s} \leq 1960 \text{ GeV}$  and the region of the momentum transfer  $0.0008 \leq -t \leq 9.75 \text{ GeV}^2$

TABLE I: Experimental data of the electromagnetic form factor)

$N$ points	Proton	References
111	$G_E^p$	[37-43]
196	$G_M^p$	[37,39,40,44-46]
87	$\mu G_E^p/G_M^p$	[38-43]
		[38,39,44,47-49]
	neutron	
13	$G_E^n$	[50-56]
38	$G_M^n$	[57,58]
6	$\mu G_E^n/G_M^n$	[59-63]
		[52,64]

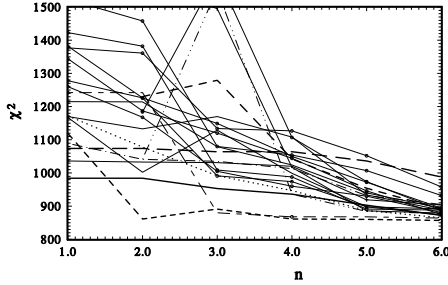


FIG. 1: The sum of  $\chi_i^2$  of the descriptions of the proton and neutron electromagnetic form factors by different PDFs over an increasing number of free parameters [Eqs. (10) and (11)].

of the elastic differential cross sections of proton-proton and proton-antiproton data [34]. So we include the whole Coulomb-hadron interference region where the experimental errors are remarkably small.

As a result, one obtains  $\sum \chi_i^2/N \simeq 1.8$ , where  $N = 975$  is the number of experimental points. Note that the parameters of the model are energy independent. The energy dependence of the scattering amplitude is determined only by the single intercept and the logarithmic dependence on  $s$  of the slope.

In the framework of this model the quantitative description of all existing experimental data at  $52.8 \leq \sqrt{s} \leq 1960$  GeV, including the Coulomb range and large momentum transfers ( $0.0008 \leq |t| \leq 9.75$  GeV<sup>2</sup>), is obtained with only three high-energy fitting parameters. Hence, the model is very sensitive to any additional contribution.

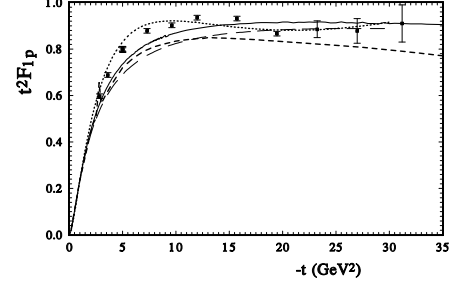


FIG. 2: Proton Dirac form factor multiplied by  $t^2$  (the hard, dotted, long-dashed, and short-dashed lines correspond to our calculations with PDFs A112, Stoller01, Rad04, and Kroll, respectively).

### III. GPDS AND FORM FACTORS OF THE NUCLEON

Further development of the model requires careful analysis of the momentum transfer form of the GPDs and a properly chosen form the PDFs. In Ref. [35], an analysis of more than 24 different PDFs was performed. We slightly complicated the form of the GPDs in comparison with Eq.(4), but it is the simplest one compared to other works (for example, Ref. [36]):

$$\mathcal{H}^u(x, t) = q(x)_{nf}^u e^{2a_H \frac{(1-x)^{2+\epsilon_u}}{(x_0+x)^m} t}; \quad (10)$$

$$\mathcal{H}_\Gamma^d(x, t) = q(x)_{nf}^d e^{2a_H(1+\epsilon_0)(\frac{(1-x)^{1+\epsilon_d}}{(x_0+x)^m}) t},$$

$$\mathcal{E}^u(x, t) = q(x)_{fl}^u e^{2a_E \frac{(1-x)^{2+\epsilon_u}}{(x_0+x)^m} t}, \quad (11)$$

$$\mathcal{E}_\Gamma^d(x, t) = q(x)_{fl}^d e^{2a_E(1+\epsilon_0)(\frac{(1-x)^{1+\epsilon_d}}{(x_0+x)^m}) t},$$

where  $q(x)_{fl}^{u,d} = q(x)_{nf}^{u,d}(1-x)^{z_1, z_2}$ .

A complex analysis of the corresponding description of the electromagnetic form factors of the proton and neutron using the different PDF sets (24 cases) was carried out. These PDFs include the leading-order, next-to-leading order, and the next-to-next-to-leading order determinations of the parton distribution functions. They used different forms of the  $x$  dependence of the PDFs. The analysis was carried out with different forms of the  $t$  dependence of the GPDs. The minimum number of free parameters was six and maximum was ten.

To obtain the form factors, we have to integrate over  $x$  in the whole range 0 – 1. Hence, the form of the  $x$  dependence of a PDF affects the form and size of the form factor. But the PDF sets are determined from the inelastic processes only in some region of  $x$ , which is only approximated to  $x = 0$  and  $x = 1$ . Some PDFs have a polynomial form of  $x$  with

TABLE II: The fitting parameters of the GPDs with flavor dependence

Model	$\epsilon_u$ $\pm 0.02$	$\epsilon_d$ $\pm 0.01$	$\epsilon_0$ $\pm 0.01$	$m$ $\pm 0.01$	$\alpha_H$ $\pm 0.03$	$\alpha_E$ $\pm 0.07$	$x_0$ $\pm 0.002$	$z_u$ $\pm 0.03$	$z_d$ $\pm 0.03$	$\chi^2_{+4p}/\chi^2_0$
ABKM09	0.11	0.2	0.09	0.42	0.45	0.57	0.004	0.67	-1.88	0.91
ABM12	0.13	0.04	0.13	0.41	0.47	0.60	0.002	0.54	-2.06	0.89

a different power. Some others have an exponential dependence on  $x$ . As a result, the behavior of the PDFs, when  $x \rightarrow 0$  or  $x \rightarrow 1$ , can influence the form of the calculated form factors.

The sets of experimental data are presented in Table I. The sets of data have various corrections and different methods which take into account the systematic errors. So we take into account only the statistical errors. On the basis of this analysis we calculated the electromagnetic form factors of the proton and neutron (using the isotopic symmetry). Then we carried out the fit of these calculations and obtained the parameters of the electromagnetic  $[G(t)]$  and matter  $[A(t)]$  form factors.

The results of the fitting procedure with different numbers of free parameters for the whole set of PDFs are presented in Fig. 1. We found that the best description was given by the PDFs from Refs. [65, 66]. In this case, the increase in the number of the free parameters leads to a small decrease in  $\chi^2$ . This means that the  $x$  dependence of the PDFs corresponds sufficiently well to the  $u$  and  $d$  distributions in the nucleon to reproduce the electromagnetic form factors. Note that these PDFs use a special power dependence on  $x$ . The most stable results (i.e., a minimum dependence on the number of free parameters with a minimum of  $\chi^2$ ) are obtained with the PDFs ABKM09 [65] and ABM12 [66] (see Table II).

The obtained form factors for the proton and neutron are shown in Fig. 2 and Fig. 3. The form factors practically coincide for both PDFs used. In Fig. 2, our results are compared with the other model calculations for  $F_1(t)$ . It should be noted that the experimental data for large  $t$  were obtained by the Rosenbluth method, and our calculations and the calculation in Ref. [36] differ slightly from the experimental data at large  $t$ , but they practically, coincide with each other. The ratio of  $\mu G_E/G_M$  for the proton and neutron cases is presented in Fig. 3. Our calculations reproduce the data obtained by the polarization method quite well.

On the basis of our GPDs with the ABM12 PDFs [66],

$$q_u(x) = \frac{4.649903x^{-0.288}(1-x)^{3.637}}{x^{0.5933x-3.607x^2+3.718x^3}}, \quad (12)$$

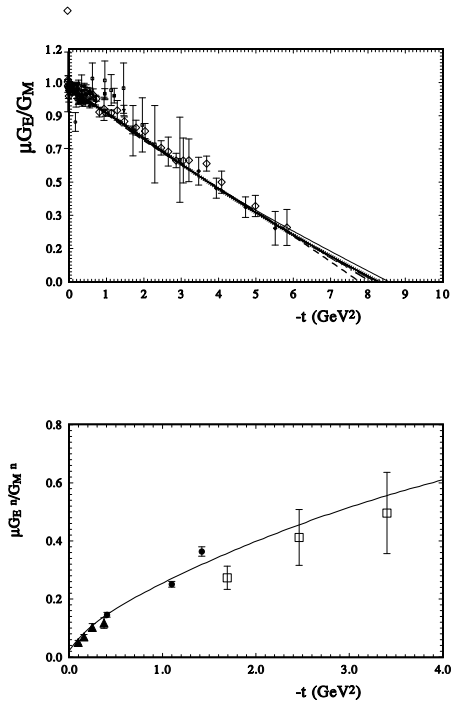


FIG. 3: The model description of the ratio of the electromagnetic form factors for the proton  $\mu_p G_E^p/G_M^p$  and for the neutron  $\mu_n G_E^n/G_M^n$ .

$$q_d(x) = \frac{3.424394x^{-0.259}(1-x)^{5.123}}{x^{1.122x-2.984x^2}}, \quad (13)$$

we calculated the hadron form factors using numerical integration,

$$F_1(t) = \int_0^1 dx \left[ \frac{2}{3} q_u(x) e^{2\alpha_H t(1-x)^{2+\epsilon_u}/(x_0+x)^m} - \frac{1}{3} q_d(x) e^{2\alpha_H t(1-x)^{1+\epsilon_d}/((x_0+x)^m)} \right] \quad (14)$$

and then by fitting these integral results with the standard dipole form with some additional paramete-

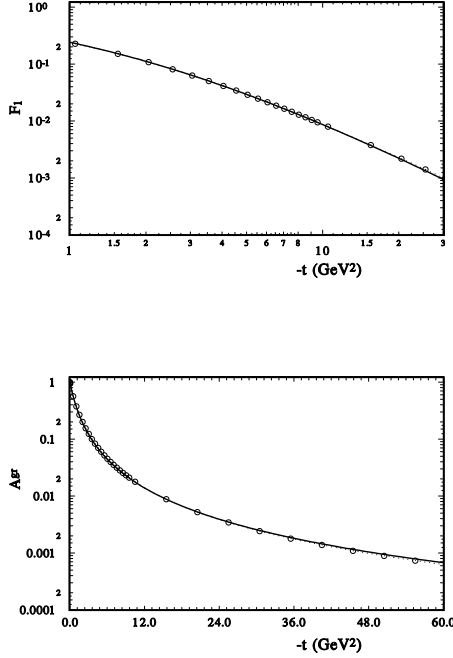


FIG. 4: The fit of the form factors of the proton: (a) (top), the electromagnetic form factor  $G(t)$  [Eq.(15)] and (bottom) the matter form factor  $A(t)$  [Eq.(17)]. The circles are the moments of the GPDs (shown only every tenth point).

ters for  $F_1(t)$ ,

$$F_1(t) = \frac{4m_p - \mu t}{4m_p - t} \frac{1}{(1 + q/a_1 + q^2/a_2^2 + q^3/a_3^3)^2} \quad (15)$$

The matter form factor

$$A(t) = \int_0^1 x \, dx \quad (16)$$

$$\left[ q_u(x) e^{2\alpha_H t(1-x)^{2+\epsilon_u}/(x_0+x)^m} + q_d(x) e^{2\alpha_H t(1-x)^{1+\epsilon_d}/((x_0+x)^m)} \right]$$

is fitted by the simple dipole form

$$A(t) = \frac{\Lambda^4}{(\Lambda^2 - t)^2}. \quad (17)$$

The results of the integral calculations and the fitting procedure are shown in Fig. 4. Our description is valid up to a large momentum transfer with the following parameters:

$a_1 = 16.7$ ,  $a_2^2 = 0.78$ ,  $a_3^3 = 12.5$  and  $\Lambda^2 = 1.6$ . These form factors will be used in our model of the proton-proton and proton-antiproton elastic scattering.

#### IV. EXTENSION OF THE HEGS MODEL

The obtained form factors differ slightly from those used in our previous work [24]. Hence, we have to make a new fit of high-energy data, including now the new data of the TOTEM Collaboration [8, 67]. As was noted in our previous work, the model also describes low-energy data qualitatively. Now we include in our fitting procedure additional experimental data on the  $pp$  and  $p\bar{p}$  elastic scattering up to  $8 \text{ TeV} \geq \sqrt{s} \geq 9.8 \text{ GeV}$ . As a result, the amount of experimental data increases by a factor of 3.5 (from 980 to 3416). This gives us many experimental high-precision data points at small momentum transfer, including the Coulomb-hadron interference region where the experimental errors are remarkably small. Hence, we can check our model construction where the real part is determined only by the complex representation of  $\hat{s} = s/s_0 \exp(-i\pi/2)$ . We do not include the data on the total cross sections  $\sigma_{\text{tot}}(s)$  and  $\rho(s)$ , as their values were obtained from the differential cross sections, especially in the Coulomb-hadron interference region. Including such data decreases  $\chi^2$ , but it would be double counting in our opinion. We also do not include the interpolated and extrapolated data of Amaldi [68], and only include their original experimental data.

As in the old version of the model, we take into account only the statistical errors in the standard fitting procedure. The systematic errors are taken into account by the additional normalization coefficient which is the same for every row of the experimental data. It essentially decreases the space of the possible form of the scattering amplitude. Of course, it is necessary to control the sizes of the normalization coefficients so that they do not introduce an additional energy dependence. As we will see later (Tables III and IV), the distribution of the coefficients has the correct statistical properties and does not lead to a visible additional energy dependence.

Such a simple form of the scattering amplitude in the huge region of energy requires careful determination of the slope of the scattering amplitude. As was noted in Ref. [7]), analytic  $S$ -matrix theory, perturbative quantum chromodynamics, and the data require that Regge trajectories be nonlinear complex functions [69, 70]. The Pomeron trajectory has threshold singularities, the lowest one being due to the two-pion exchange, required by the  $t$ -channel unitarity Ref. [71]. This threshold singularity appears in different forms in various models (see [7]).

In the present model, a small additional term is introduced into the slope which reflects some possible small nonlinear properties of the intercept. As a result, the slope is taken in the form

$$B(s, t) = (\alpha_1 + kq e^{-kq^2 L n(\hat{s} \, t)}) L n(\hat{s}). \quad (18)$$

This form leads to the standard form of the slope as  $t \rightarrow 0$  and  $t \rightarrow \infty$ . Note that our additional term

at large energies has a similar form as an additional term to the slope coming from  $\pi$  loop examined in Ref. [71] and recently in Ref. [72]. The basic Born amplitudes were taken in the old form, [Eqs. (5) and (6)] with fixed  $\alpha_1 = 0.24 \text{ GeV}^{-2}$  and  $\Delta = 0.11$ . Taking into account the Mandelstam region of the analyticity scattering amplitude for the  $2 \rightarrow 2$  scattering process  $s + u + t = 4m_p^2$  we take  $s_0 = 4m_p^2$  where  $m_p$  is the mass of the proton.

Then, as we intend to describe sufficiently low energies, possible Odderon contributions were taken into account:

$$F_{\text{odd}}(s, t) = \pm h_{\text{odd}} A^2(t) F_b(s, t), \quad (19)$$

where  $h_{\text{odd}} = ih_3 t / (1 - r_0^2 t)$ .

Just as we supposed in the previous variant of the HEGS model that  $F_b(s, t)$  corresponds to the cross-even part of the three gluon exchange, our Odderon contribution is also connected with the matter form factor  $A(t)$ . Our ansatz for the Odderon slightly differs from the cross-even part by some kinematic function. The form of the Odderon working in all  $t$  has the same behavior as the cross-even part at larger momentum transfer, of course, with different signs for proton-proton and proton-antiproton reactions. It has a large preasymptotic part, and as a result, such a preasymptotic part of the cross-even part is practically not felt. Hence, the Born term of the elastic hadron amplitude can now be written as

$$\begin{aligned} F_h^{\text{Born}}(s, t) = & h_1 F_1^2(t) F_a(s, t) (1 + r_1/\hat{s}^{0.5}) \\ & + h_2 A^2(t) F_b(s, t) \\ & \pm h_{\text{odd}} A^2(t) F_b(s, t) (1 + r_2/\hat{s}^{0.5}), \end{aligned} \quad (20)$$

where  $F_a(s, t)$  and  $F_b(s, t)$  are the same as in the previous variant of the model [see Eq. (6)].

The analysis of the hard Pomeron contribution in the framework of the model [25] shows that such a contribution is not felt. For the most part, the fitting procedure requires a negative additional hard Pomeron contribution. We repeat the analysis of [25] in the present model and obtain practically the same results. Hence, we do not include the hard Pomeron in the model.

At large  $t$  our model calculations are extended up to  $-t = 15 \text{ GeV}^2$ . We added a small contribution from the energy-independent part of the spin-flip amplitude in a form similar to that proposed in Ref. [73].

$$F_{sf}(s, t) = h_{sf} q^3 F_1^2(t) e^{-B_{sf} q^2}. \quad (21)$$

It has two additional free parameters. Of course, at lower energy we need to take into account the energy-dependent parts of the spin-flip amplitudes. However, this requires including additional polarization data in our examination which essentially complicates the picture. This is beyond the scope of this paper. Such a contribution can be made in future

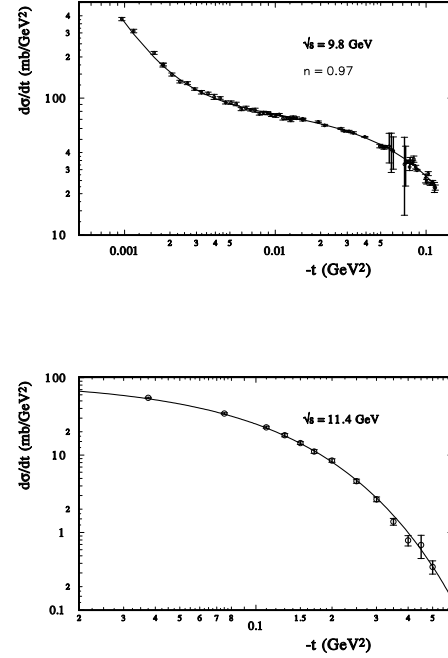


FIG. 5:  $d\sigma/dt$  for  $pp$  (top) at  $\sqrt{s} = 9.8 \text{ GeV}$  and  $p\bar{p}$  (bottom) at  $\sqrt{s} = 11.3 \text{ GeV}$ .

works. The model is very simple from the viewpoint of the number of fitting parameters and functions. There are no artificial functions or any cuts which bound the separate parts of the amplitude by some region of momentum transfer.

## V. ANALYSIS AND RESULTS

We included 3416 experimental points were included in our analysis in the energy region  $9.8 \text{ GeV} \leq \sqrt{s} \leq 8 \text{ TeV}$  and in the region of momentum transfer  $0.000375 \leq |t| \leq 15 \text{ GeV}^2$ . The experimental data of the proton-proton and proton-antiproton elastic scattering are included in 92 separate rows of 32 experiments [34], including recent data from the TOTEM Collaboration at  $\sqrt{s} = 8 \text{ TeV}$  [67]. The whole Coulomb-hadron interference region, where the experimental errors are remarkably small, was included in our examination of the experimental data (see Tables III and IV).

In the fitting procedure by FUMILIM program [74] we calculated the minimum in  $\sum_{i=1}^N \chi_i^2$  related to the statistical errors  $\sigma_i^2$ . The systematic errors are taken into account by the additional normalization coefficient  $n_k$  for the  $k$  series (the experiment) of experimental data,

$$\chi^2 = \sum_{i=1}^N \frac{n_k E_i^k(s, t) - T_i(s, t)}{\sigma_i^2(s, t)}, \quad (22)$$

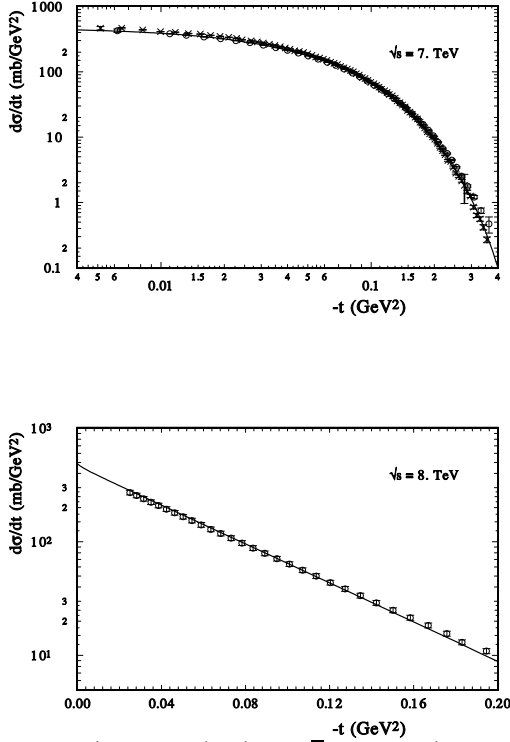


FIG. 6:  $d\sigma/dt$  for  $pp$  (top) at  $\sqrt{s} = 7$  TeV (crosses and circles are TOTEM [77] and ATLAS [78] data, respectively) and (bottom) at  $\sqrt{s} = 8$  TeV (circles are TOTEM data [67])

where  $T_i(s, t)$  are the theory predictions, including the hadronic and electromagnetic parts of the scattering amplitude, and  $n_k E_i(s, t)$  are the data points allowing a shift by the systematical error of the  $k$  experiment (see, for example, Refs. [75, 76]).

In the region of small momentum transfer the systematic errors are on the order of 2 – 5%. For the most part, the additional normalization is in the region 0.95 – 1.05. At large momentum transfer the order of the systematical errors is 10 – 20%. In this case, the additional normalization is situated in the region 0.8 – 1.2. Of course, if one sums the systematic and statistical errors,  $\sum \chi^2/N$  decreases but it will give some additional space for changing the form of the scattering amplitude.

Our complete fit of 3416 experimental data points in the energy range  $9.8 \leq \sqrt{s} \leq 8000$  GeV and the region of momentum transfer  $0.000375 \leq -t \leq 14.75$  GeV<sup>2</sup> gives  $\sum_{i=1}^N \chi_i^2/N = 1.28$ , with the parameters  $h_1 = 3.67$ ;  $h_2 = 1.39$ ;  $h_{\text{odd}} = 0.76$ ;  $k_0 = 0.16$ ;  $r_0^2 = 3.82$ , and the low-energy parameters  $h_{sf} = 0.05$ ;  $r_1 = 53.7$ ;  $r_2 = 4.45$ .

Obviously, for such a huge energy region we have a very small number of free parameters. We also note the good description of the CNI region of momentum transfer in a very wide energy region (approximately 3 orders of magnitude) with the same slope of the scattering amplitude. The differential cross

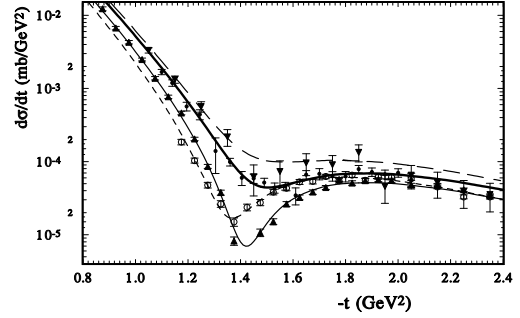


FIG. 7: The form and energy dependence of the diffraction minimum at low energies (long-dashed line:  $\sqrt{s} = 13.4$  GeV; thick hard line:  $\sqrt{s} = 18.4$  GeV; hard line:  $\sqrt{s} = 30.4$  GeV; dashed line:  $\sqrt{s} = 44.7$  GeV).

sections of the proton-proton and proton-antiproton elastic scattering at small momentum transfer are presented in Fig. 5 at  $\sqrt{s} = 9.8$  GeV for  $pp$  scattering, and  $\sqrt{s} = 11$  GeV for  $p\bar{p}$  elastic scattering, and in Fig. 6 at  $\sqrt{s} = 7$  TeV and  $\sqrt{s} = 8$  TeV for  $pp$  scattering. The model quantitatively reproduces the differential cross sections in the whole examined energy region in spite of the fact that the size of the slope is essentially changing in this region [due to the standard Regge behavior  $\log(\hat{s})$  and the real part of the scattering amplitude has different behaviors for  $pp$  and  $p\bar{p}$ ].

The results for the whole energy region for small momentum transfer are presented in Table III for the proton-proton elastic scattering and in Table IV for the proton-antiproton elastic scattering. We can see that the  $\chi^2$  values are suitable. We note that they are especially small for the high-precision FNAL-JINR data which reach a very small size of the momentum transfer (up to  $-t = 0.00037$  GeV<sup>2</sup> [79] at energies  $\sqrt{s} = 13.4, 19.4, 23.4$ , and 27.4 GeV. The additional normalization coefficients do not show an energy dependence and are distributed only statistically. We also include the high-precision non-normalized data of the UA4/2 Collaboration at  $\sqrt{s} = 541$  GeV which reach a very small momentum transfer  $-t_{\text{min}} = 0.000875$  GeV<sup>2</sup>.

The real part of the scattering amplitude significantly influences the size and form of the differential cross sections in the Coulomb-hadron interference region [80, 81]. The second Reggeons also have a large slope for the imaginary part and hardly change the slope of the differential cross sections. A suitable description of both  $pp$  and  $p\bar{p}$  experimental data in this region supports the determination of the real part of the scattering amplitude chosen in the model. It should be noted that possible contributions of the second Reggeons will essentially change the form and size of the real part of the scattering amplitude. The results presented in Tables III and IV show that up to such a low energy we do not feel

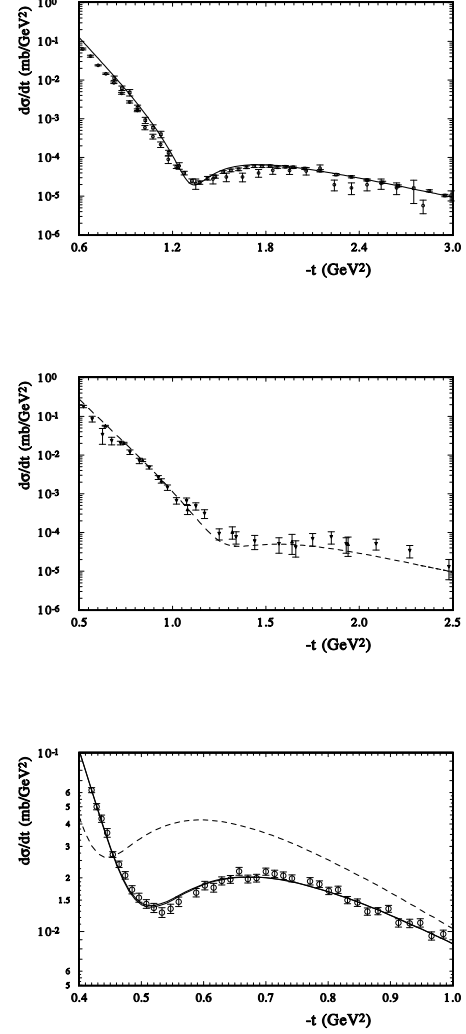


TABLE III: The proton-proton elastic scattering at small  $t$ 

$\sqrt{s}$ , GeV	$t_{\min}$ , GeV	$t_{\max}$ , GeV	N	$\sum_N \chi^2$	$\sum_N \chi^2/N$	$n_k$ (norm.)
9.0	0.00193	0.04328	19	14.4	0.72	1.041
9.3	0.01268	0.1147	28	21	0.75	1.019
9.8	0.00115	0.115	64	87.6	1.35	1.013
9.8	0.0026	0.12	23	31.0	1.37	1.074
9.9	0.00063	0.0306	73	81.1	1.11	1.014
10.6	0.00079	0.01529	45	68.0	1.39	1.026
12.3	0.00066	0.02928	58	46.9	0.81	1.018
13.76	0.0023	0.0388	73	84.9	1.16	1.023
13.76	0.035	0.095	7	2.5	0.36	1.029
16.83	0.0022	0.0392	68	76.9	1.13	1.006
19.42	0.00066	0.0315	69	79.5	1.15	0.996
19.42	0.035	0.095	7	12.2	1.74	1.008
19.42	0.0206	0.12	42	19.9	0.47	1.038
21.7	0.022	0.039	64	50.1	0.78	0.996
22.2	0.0005	0.02978	64	55.6	0.87	1.007
23.5	0.00037	0.0102	30	58.5	1.95	1.008
23.8	0.0022	0.0388	60	69.1	1.15	1.001
23.9	0.00066	0.0316	66	76.5	1.16	0.988
27.4	0.00047	0.02579	61	66.1	1.08	0.987
30.6	0.016	0.11	48	53.1	1.10	1.005
30.8	0.0005	0.0176	31	75.7	2.36	1.009
44.7	0.00099	0.01856	40	51.	1.16	1.004
52.8	0.00107	0.05546	35	53.2	1.52	1.016
62.3	0.00543	0.05122	23	31.7	1.38	1.005
7000.	0.00515	0.356	84	173.4	2.04	0.943
7000.	0.006	0.36	40	31.4	0.77	1.0
8000.	0.028	0.195	30	20	0.7	0.9

TABLE IV: The proton-antiproton elastic scattering at small  $t$ 

$\sqrt{s}$ , GeV	$t_{\min}$ , GeV	$t_{\max}$ , GeV	N	$\sum_N \chi^2$	$\sum_N \chi^2/N$	$n_k$ (norm.)
11.54	0.0375	0.5	13	11.5	0.88	0.983
13.76	0.035	0.095	7	7.4	1.06	0.966
19.42	0.035	0.095	7	7.3	1.05	1.220
30.4	0.00067	0.01561	28	28.8	1.03	0.974
52.6	0.00097	0.03866	28	24.5	0.875	0.987
52.8	0.0109	0.0479	43	49.9	1.16	0.933
62.3	0.00632	0.03821	43	55.8	1.3	0.996
541.	0.000875	0.11875	99	164.7	1.65	unnorm.
546.	0.00225	0.03475	66	83.7	1.25	1.004
546.6	0.026	0.078	14	13.86	1.0	1.002
1800.	0.0339	0.285	28	28.8	1.03	1.024

FIG. 8:  $d\sigma/dt$  for  $pp$  at  $\sqrt{s} = 52.8$  GeV (top), and  $p\bar{p}$  at  $\sqrt{s} = 52.8$  GeV (middle), and  $pp$  at  $\sqrt{s} = 7$  TeV (bottom) [the dashed line (bottom) is the predictions at  $\sqrt{s} = 14$  TeV].

the essential contributions of the second Reggeons. This especially concerns the possible contribution of the  $f_0$  meson. In some models it has an intercept essentially above 0.5 and its contribution influences the differential cross sections and  $\sigma_{\text{tot}}(s)$  and  $\rho(s, t)$  in the ISR energy region. Our results practically exclude such Reggeons with an intercept above 0.5.

The form and energy dependence of the diffraction minimum are very sensitive to the different parts of the scattering amplitude. The change of the sign of the imaginary part of the scattering amplitude determines the position of the minimum and its movement with a change in the energy. The real part of the scattering amplitude determines the size of the dip. Hence, it depends heavily on the Odderon contribution. The spin-flip amplitude gives the con-

tribution in the differential cross sections additively. So the measurement of the form and energy dependence of the diffraction minimum with high precision is an important task for future experiments. In Fig. 7, the description of the diffraction minimum in our model is shown for low energies. The HEGS model sufficiently reproduces the energy dependence and form of the diffraction dip. In this energy region the diffraction minimum reaches the sharpest dip at  $\sqrt{s} = 30$  GeV. Note that at this energy the value of  $\rho(s, t = 0)$  also changes its sign in the proton-proton scattering. The  $p\bar{p}$  cross sections in the model are obtained by the  $s \rightarrow u$  crossing without changing the model parameters. And for the proton-antiproton scattering the same situation with correlations between the sizes of  $\rho(s, t = 0)$  and  $\rho(s, t_{\min})$  takes place at low energy (approximately at  $p_L = 50$  GeV). Such a correlation was noted in Ref. [82].

The model reproduces  $d\sigma/dt$  at very small and large  $t$  and provides a qualitative description of the dip region at  $-t \approx 1.4$  GeV<sup>2</sup>, for  $\sqrt{s} = 53$  GeV and for  $\sqrt{s} = 62.1$  GeV for the proton-proton and proton-antiproton elastic scattering (see top and middle panels of Fig.8). The diffraction minimum at  $\sqrt{s} = 7$  TeV is reproduced sufficiently well too (see Fig.8c).

In Fig. 9, the description of the differential cross sections of the elastic scattering  $pp$  at large  $t$  and different values of  $s$  is presented. It is to be noted that the calculation of our integrals with complex oscillation functions at large momentum transfer is a difficult task and requires high-precision of the calculations. In any case, we obtain a quantitatively good description of the differential cross sections at large  $t$ . In this region of  $t$ , the contribution of the spin-flip amplitude is felt. We take into account only the asymptotic part of this amplitude with the simplest and energy-independent forms. Although it has a small size, its constant is determined sufficiently well,  $h_{sf} = 0.06 \pm 0.004$ .

In Fig. 10, the model calculations for the differential cross sections are shown for the LHC energies. Obviously, in the model the difference in the behavior of the differential cross sections between  $\sqrt{s} = 7$  and  $\sqrt{s} = 14$  TeV is not large. For the most part, it is reflected in the movement of the position of the diffraction minimum to low momentum transfer and the increase of the sizes of the differential cross sections in the minimum and second diffraction maximum.

## VI. THE STRUCTURE OF THE SCATTERING AMPLITUDE

In the model, only the Born terms of the scattering amplitude are determined. The separate terms and the full Born scattering amplitude have a sim-

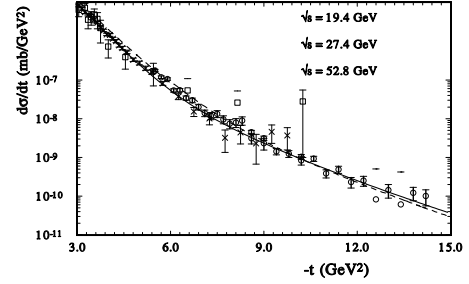


FIG. 9:  $d\sigma/dt$  at large  $t$  for  $pp$  at  $\sqrt{s} = 19.4$  GeV (hard line),  $\sqrt{s} = 27.4$  GeV, and  $\sqrt{s} = 52.8$  GeV (dashed line). The squares, circles, crossing are the experimental data for each case, respectively.

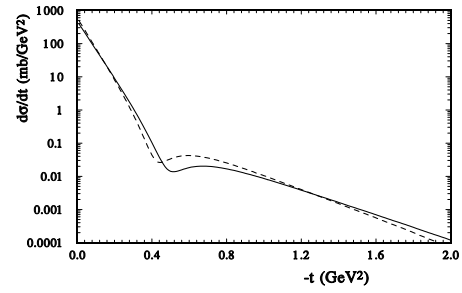


FIG. 10: The model predictions of  $d\sigma/dt$  at  $\sqrt{s} = 7$  (hard line) and  $\sqrt{s} = 14$  TeV (dashed line).

ple form and their imaginary parts do not have any oscillating behavior at small momentum transfer. In Fig. 11 and Fig. 12, the parts of the Born terms of the scattering amplitude are presented at  $\sqrt{s} = 9.8$  GeV and  $\sqrt{s} = 7$  TeV. At small momentum transfer the imaginary part of the Pomeron  $P_{2g}$  dominates at both energies. At small energy, the cross-even and cross-odd imaginary parts of  $P_{3g}$  are equal to  $P_{2g}$  in the region of momentum transfer  $0.7 - 0.9$  GeV<sup>2</sup>, and then they dominate. Both parts of  $P_{3g}$  have the same size at  $-t > 1$  GeV<sup>2</sup>. But the real part of the cross-odd term of  $P_{3g}$  dominates at  $-t > 0.4$  GeV<sup>2</sup> and determines the real part of the full Born term of the scattering amplitude. As it has a different sign, compared to the real part of  $P_{2g}$ , the full real part of the Born term changes the sign at  $-t = 0.3$  GeV<sup>2</sup>.

At  $\sqrt{s} = 7$  TeV the picture is different. In this case, the imaginary part of the cross-odd  $P_{3g}$  practically does not influence the form of the scattering amplitude. The imaginary part of the cross-even  $P_{3g}$  exceeds the imaginary part of  $P_{2g}$  when  $-t > 0.3$  GeV<sup>2</sup> and further determines the full Born term.

The energy dependence of the imaginary and real parts of the full Born term of the scattering ampli-

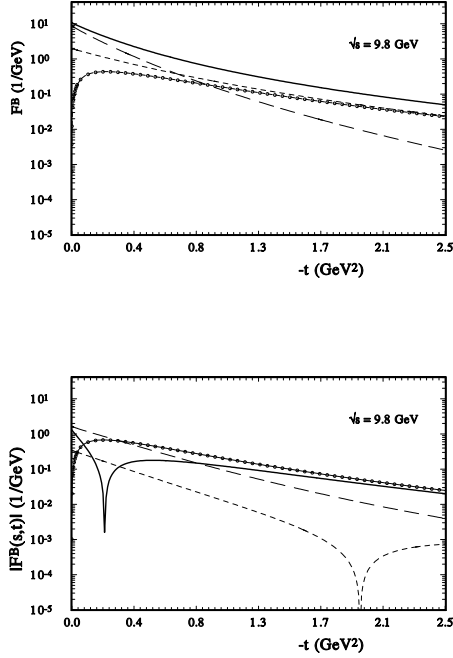


FIG. 11: The magnitude of the Born parts of the  $pp$  elastic scattering amplitudes at  $\sqrt{s} = 9.8$  GeV. (Top) The imaginary parts: the sum of all parts (hard line), the contribution of  $P_{2g}$  (long-dashed line), the contribution of the cross-even  $P_{3g}$  (dashed line), and the contribution of the cross-odd part of  $P_{3g}$  (line with points). (Bottom) The same for the real parts of the Born amplitude.

tude is shown in Fig. 13. Note that the imaginary part grows with energy at small and decreases at large momentum transfer. The real part changes the sign and then grows at small momentum transfer but has a small energy dependence at large  $t$ .

The energy dependence of the slope of the full Born term of the scattering amplitude is represented in Fig. 14. As  $\hat{s}$  is complex, the slope has the real and imaginary parts too. The slope changes with  $s$  most quickly at small momentum transfer. The minimum change occurs in the region  $-t \approx 0.8$  GeV<sup>2</sup>. In Fig. 15, the energy dependence of the "basic" slope  $B(s, t)$  [Eq.(18)] is shown. Its real part has a simple form at low energies with a growing maximum at high energies that moves towards low  $t$ . However, the imaginary part has a more complicated energy dependence. The maximum of its energy dependence occurs at a momentum transfer larger than that for the real part in the region  $0.4 < -t < 0.8$  GeV<sup>2</sup>. The distinction of the form of the slope from the constant (linear) slope cannot be explained by the absence of the second Reggeons in the model. The second Reggeons have real and imaginary parts of the same order with a large slope near  $\alpha_1 \approx 0.9$  GeV<sup>-2</sup>. They essentially change the  $t$  dependence

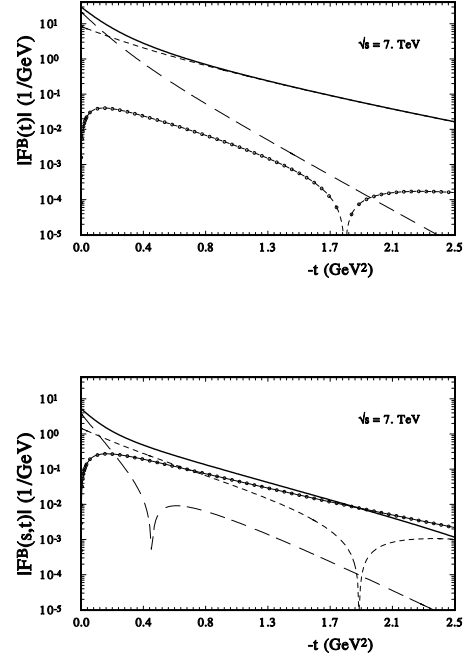


FIG. 12: The magnitude of the Born parts of the  $pp$  elastic scattering amplitudes at  $\sqrt{s} = 7$  TeV. (Top) The imaginary parts: the sum of all parts (hard line), the contribution of  $P_{2g}$  (long-dashed line), the contribution of the cross-even  $P_{3g}$  (dashed line), and the contribution of the cross-odd part of  $P_{3g}$  (line with points). (Bottom) The same for the real parts of the Born amplitude.

of the differential cross sections at low momentum transfer and especially in the CNI region.

In order to use the unitarization procedure, it is necessary to transform the Born term of the scattering amplitude in the impact-parameter presentation. As our Born term has the form factor in a complicated form compared to the simple exponential, this transform can be performed only by numerical integration, [Eq.(7)]. Then, the standard eikonal representation is used to obtain the overlapping function in the impact-parameter representation, [Eqs. (8 and 9)].

The energy dependence of the corresponding term of  $\Gamma(s, b)$  eq.(9) is represented in Fig. 16. One can see that the black disc limit is not reached at  $\sqrt{s} = 7$  TeV [where  $Im \Gamma(s, b = 0) = 0.93$ ] and even at  $\sqrt{s} = 14$  TeV [where  $Im \Gamma(s, b = 0) = 0.95$ ]. The real part of  $\Gamma(b, s)$  (bottom panel of Fig. 16) is small and has some important influence only at large impact parameters. Hence, the behavior of the scattering amplitude will change to the saturation regime when the energy grows essentially above the LHC energies. It is necessary to take this into account when the cross sections are extrapolated from the accelerator energies to the energies reached in cosmic-ray

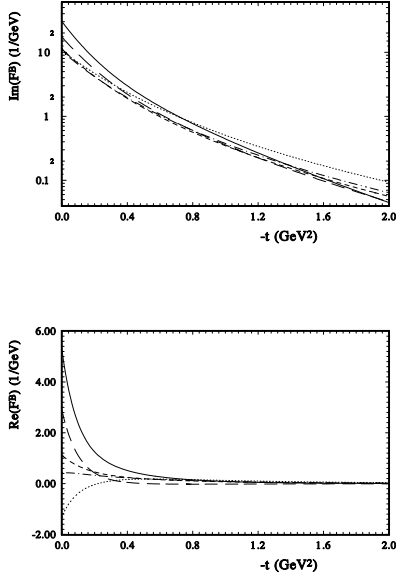


FIG. 13: (Top) panel] The imaginary part of the full Born amplitude of the the  $pp$  elastic scattering amplitudes at  $\sqrt{s} = 7$  TeV (solid line),  $\sqrt{s} = 541$  GeV (long-dashed line),  $\sqrt{s} = 52.8$  GeV (dashed line),  $\sqrt{s} = 27.4$  GeV (dashed-dotted line),  $\sqrt{s} = 9.8$  GeV (dotted line). (Bottom) The same for the real parts of the Born amplitude.

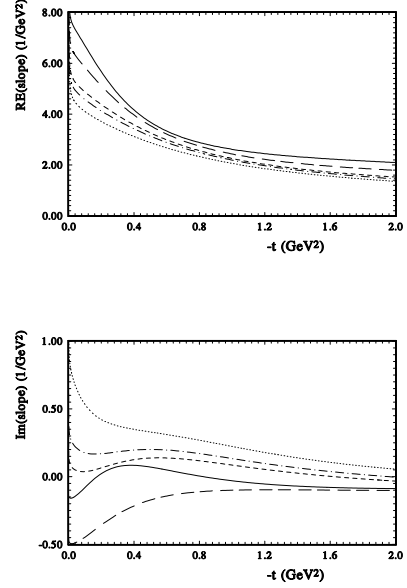


FIG. 14: (Top) The real part of the slope of the full Born amplitude of the the  $pp$  elastic scattering amplitudes at  $\sqrt{s} = 7$  TeV (solid line),  $\sqrt{s} = 541$  GeV (long-dashed line),  $\sqrt{s} = 52.8$  GeV (dashed line),  $\sqrt{s} = 27.4$  GeV (dashed-dotted line),  $\sqrt{s} = 9.8$  GeV (dotted line). (Bottom) The same for the real parts of the Born amplitude.

experiments.

The corresponding representations for the total, elastic and inelastic cross sections are

$$\sigma_{\text{tot}}(s) = 2 \int b \Gamma_{\text{tot.}}(s, b) db, \quad (23)$$

with  $\Gamma_{\text{tot}}(s, b) = \text{Re}\{1 - \exp[\chi(s, b)]\}$ ,

$$\sigma_{\text{el}}(s) = \int b \Gamma_{\text{el}}(s, b) db, \quad (24)$$

with  $\Gamma_{\text{el}}(s, b) = \text{Re}\{1 - \exp[\chi(s, b)]\}^2$ , and

$$\sigma_{\text{inel}}(s) = \int b \Gamma_{\text{inel}}(s, b) db, \quad (25)$$

with  $\Gamma_{\text{inel}}(s, b) = \text{Re}\{1 - \exp[2\chi(s, b)]\}$ .

The energy and impact parameter dependence of these values are represented in Fig. 17. The  $\Gamma_{\text{inel}}(s, b)$  saturates the unitarity bound up to  $b = 0.6$  fm at  $\sqrt{s} = 14$  TeV. However,  $\Gamma_{\text{el}}(s, b)$  and the corresponding  $\Gamma_{\text{tot}} = \Gamma_{\text{el}} + \Gamma_{\text{inel}}$  do not reach the unitarity bound at this energy. In the middle panel of Fig. 17, we can see that such saturation takes place only at very large energy,  $\sqrt{s} = 100$  TeV. As a result, the maximal growth of  $\Delta\Gamma_{\text{inel}}(s_2, s_1) = \Gamma_{\text{inel}}(s_2) - \Gamma_{\text{inel}}(s_1)$  occurs at large impact parameters. The difference between  $\Delta\Gamma_{\text{inel}}(s_2, s_1)$ ,  $\Delta\Gamma_{\text{el}}(s_2, s_1)$  and  $\Delta\Gamma_{\text{tot}}(s_2, s_1)$  of these values between  $\sqrt{s} = 14$  TeV

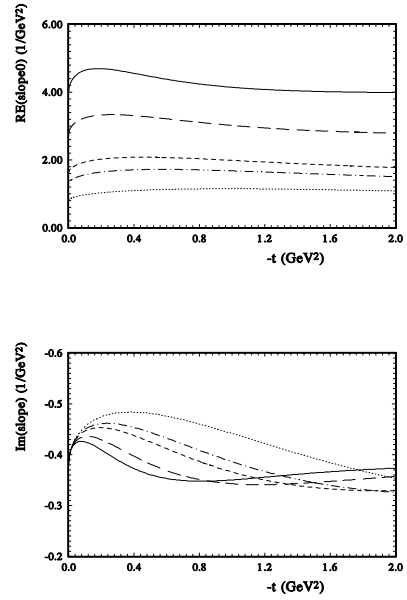


FIG. 15: a) (Top) The real part of  $B(s, t)$  [Eq.(18)] of the the  $pp$  elastic scattering amplitudes at  $\sqrt{s} = 7$  TeV (solid line),  $\sqrt{s} = 541$  GeV (long-dashed line),  $\sqrt{s} = 52.8$  GeV (dashed line),  $\sqrt{s} = 27.4$  GeV (dashed-dotted line),  $\sqrt{s} = 9.8$  GeV (dotted line), b) (Bottom) The same for the imaginary parts of  $B(s, t)$  [Eq.(18)].

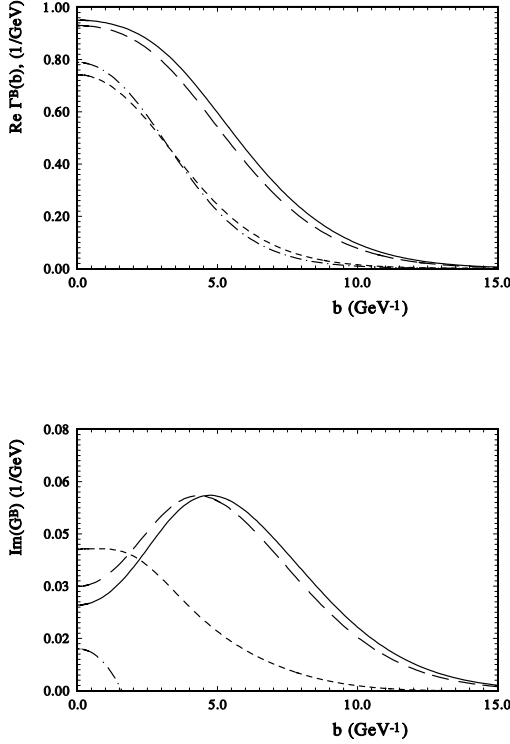


FIG. 16: The overlapping function  $\Gamma(s, b)$  [for the real (top) and imaginary (bottom) parts] at  $\sqrt{s} = 9.8$  GeV (dashed line),  $\sqrt{s} = 52.8$  GeV (dash-dotted line),  $\sqrt{s} = 7$  TeV (long dashed line),  $\sqrt{s} = 14$  TeV (hard line).

and  $\sqrt{s} = 7$  TeV is shown in the bottom panel of Fig. 17. Though the size of the growth for the elastic and inelastic values is very similar, the maximum of the growth takes place at different impact parameters. The growth of inelastic processes has a peripheral character. However, it is due to the saturation of such processes in the central region.

The full elastic scattering amplitude is calculated by numerical integration [Eq.(8)]. The magnitude of the real and imaginary parts of the full elastic scattering amplitude are represented in Fig. 18 for  $\sqrt{s} = 9.8$  GeV to  $\sqrt{s} = 7$  TeV. The imaginary part changes by moving its zero from  $-t = 1.35$  GeV<sup>2</sup> to  $-t = 0.5$  GeV<sup>2</sup>. The magnitude of the real part has zeroes in the examined region of  $t$  and mostly changes its size, but conserves its form.

It should be noted that the real part is negative at small momentum transfer at  $\sqrt{s} = 9.8$  GeV. The energy dependence of  $\rho(s, t = 0)$  (the ratio of the real part to the imaginary part of the scattering amplitude) is shown in Fig. 19. Note that we do not include the experimental data on  $\rho(s, t = 0)$  and  $\sigma_{tot}(s)$  in the fitting procedure.

In Fig. 20, the slopes of the hadronic part of the full elastic scattering amplitude are represented at

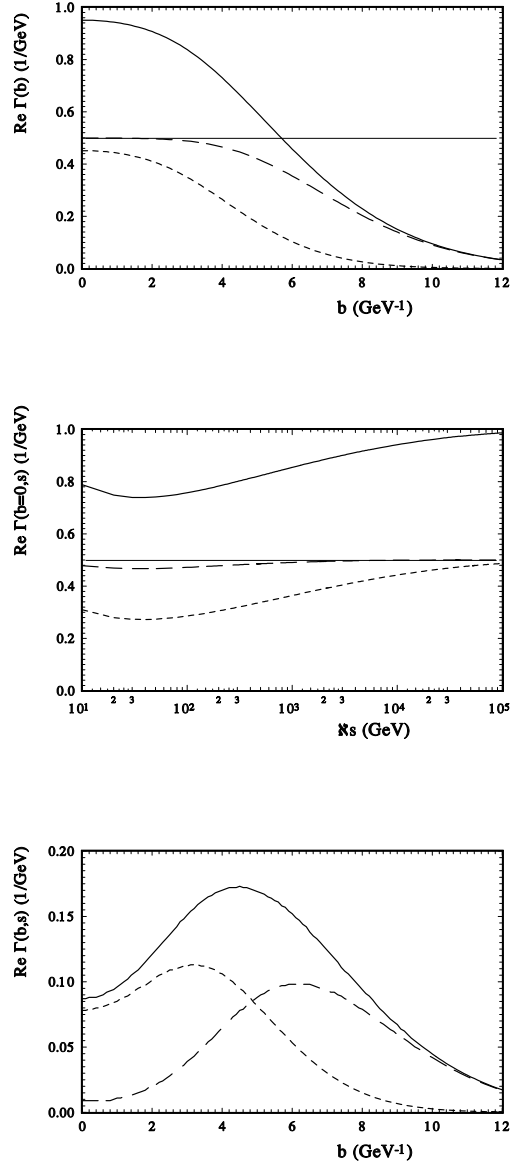


FIG. 17: (Top)  $\Gamma(s, b)_{tot}$  (hard line),  $\Gamma(s, b)_{el}$  (dashed line),  $\Gamma(s, b)_{inel}$  (long dashed line) at  $\sqrt{s} = 14$  TeV. (Middle) The energy dependence of  $\Gamma(s, b = 0)_{tot}$  (hard line),  $\Gamma(s, b = 0)_{el}$  (dashed line),  $\Gamma(s, b = 0)_{inel}$  (long dashed line). (Bottom) The differences between  $\Gamma(s, b)_{tot}$  (hard line),  $\Gamma(s, b)_{el}$  (dashed line),  $\Gamma(s, b)_{inel}$  (long dashed line) between  $\sqrt{s} = 14$  TeV -  $\sqrt{s} = 7$  TeV.

$\sqrt{s} = 9.8$  GeV and  $\sqrt{s} = 7$  TeV. Obviously, the difference between the slopes at small momentum transfer is only in the size, though we examined such different energies. The nonlinear behavior of the slope of the Born term of the scattering amplitude is very weakly reflected in the form of the slope of the eikonalized amplitude, but it essentially influences the fitting procedure. In a larger region of

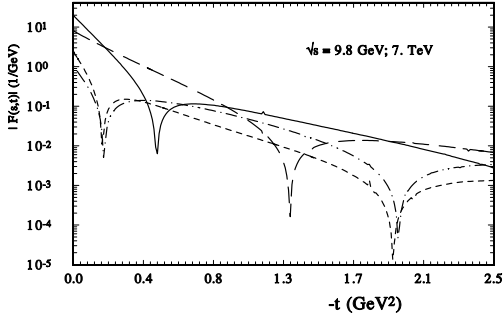


FIG. 18: The magnitude of the  $pp$  elastic scattering amplitudes after eikonalization of the imaginary part and real parts for  $\sqrt{s} = 9.8$  GeV (long-dashed line and dash-dotted line, respectively); and for  $\sqrt{s} = 7$  TeV (hard line and dashed line, respectively).

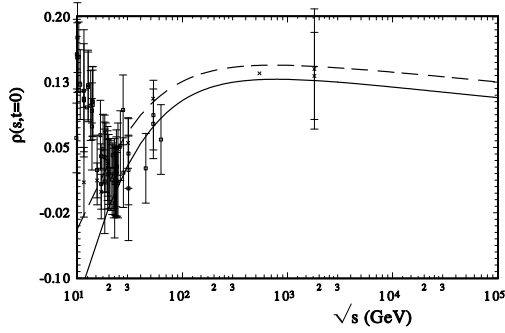


FIG. 19: The energy dependence of  $\rho(s, t = 0)$  (the ratio of the real and imaginary parts of the scattering amplitude for  $pp$  (solid line) and  $\bar{p}p$  (dashed line) scattering. We also show the experimental data for  $pp$  (squares) and  $\bar{p}p$  (crosses) scattering from Ref. [34].

the momentum transfer the slope of the differential cross section has a significant difference for the low and high energies (bottom panel of Fig. 20). This is the result of the eikonalization procedure which is reflected in the position of the diffraction minimum.

The comparison of the energy dependence of the model calculations of the slope of the differential cross sections is represented in Fig. 21. In Ref. [84], the slope was determined as

$$B_{el}(s) = \frac{\int d^2b \, b^2 \Gamma(s, b)}{\int d^2b \, b \Gamma(s, b)}; \quad (26)$$

This gives the slope at  $t = 0$ , but the experimental data for the slope are obtained at small momentum transfer and beyond the Coulomb-hadron interference region and in some region of  $t$ . So, we used the

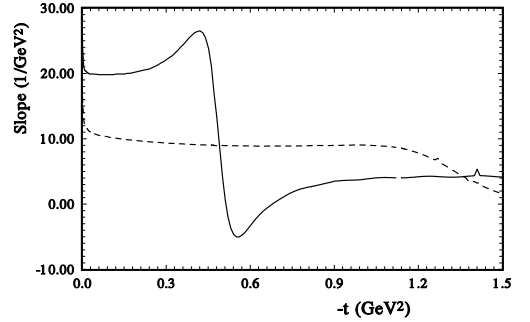
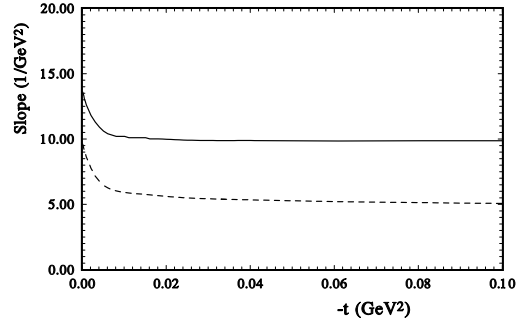
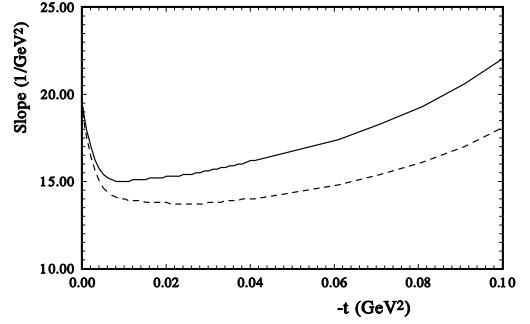


FIG. 20: The slope of the full scattering amplitude at  $\sqrt{s} = 9.8$  GeV (dashed line) and  $\sqrt{s} = 7$  TeV (hard line), for the real parts (top), the imaginary parts (middle), and the slope of the differential cross sections (bottom).

standard determination of the slope,

$$B_{el}(s) = \text{Log} \left[ \frac{d\sigma/dt|_{t_1}}{d\sigma/dt|_{t_2}} \right] / [|t_2| - |t_1|]; \quad (27)$$

In the different experimental data,  $t_1$  and  $t_2$  are different. We take some middle points:  $-t_1 = 0.04$   $\text{GeV}^2$  and  $-t_2 = 0.05$   $\text{GeV}^2$ . The experimental data have large errors. However, the energy dependence of our calculations for the most part coincides with the energy dependence of the experimental data.

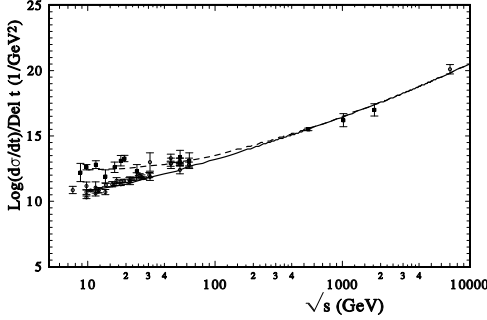


FIG. 21: The energy dependence of the forward elastic slope [Eq. (27)] compared to the existing experimental data for  $pp$  (hard line and open circles) and  $p\bar{p}$  (dashed line and squares) scattering.

## VII. CONCLUSIONS

We have presented a new model of the hadron-hadron interaction at high energies. The model is very simple with regards to the number of parameters and functions. There are no artificial functions or cuts that bound the separate parts of the amplitude by some region of momentum transfer or energy. One of the most remarkable properties is that the real part of the hadron scattering amplitude is determined only by complex energy  $\hat{s}$  that satisfies the crossing symmetries.

The new HEGS model gives a quantitative description of the elastic nucleon scattering at high energy with only five fitting high-energy parameters. Our model of the GPDs leads to a good description of the proton and neutron electromagnetic form factors and their elastic scattering simultaneously. A successful description of the existing experimental data by the model shows that the elastic scattering is determined by the generalized structure of the hadron. The model leads to a coincidence of the model calculations with the preliminary data at 8 TeV. We found that the standard eikonal approximation [85] works perfectly well from  $\sqrt{s} = 9$  GeV up to 8 TeV. The extended variant of the model shows the contribution of the "maximal" Odderon with specific kinematic properties and does not show a visible contribution of the hard Pomeron, as in Ref. [25].

The slope of the differential cross sections at small momentum transfer has a small peculiarity and has the same properties in the whole examined energy region. Such a uniform picture for the slope gives the possibility of further research into small peculiarity of different cross sections, such as possible oscillations [86]. Note that we did not see the contributions of the second Reggeons with a large slope and

TABLE V: The obtained [83] and predicted sizes of the  $\sigma_{\text{tot}}(s)$ , mb and  $\rho(t=0, s)$

$\sqrt{s}$ , GeV	$\sigma_{\text{tot-exp}}$	$\sigma_{\text{tot}}$	$\rho(t=0, s)$
19.42	$38.98 \pm 0.4$	$39.58 \pm 0.8$	$-0.005 \pm 0.0006$
22.96	$39.42 \pm 0.4$	$39.89 \pm 0.8$	$-0.005 \pm 0.0006$
52.8	$42.85 \pm 0.7$	$43.15 \pm 0.5$	$0.074 \pm 0.005$
541	$62.72 \pm 0.2$	$62.72 \pm 0.2$	$0.128 \pm 0.005$
1800	$77.3 \pm 0.38$	$77.3 \pm 0.38$	$0.127 \pm 0.02$
7000	$98.0 \pm 2.6$	$97.16 \pm 0.5$	0.121
7000	$96.4 \pm 2.$	$97.16 \pm 0.5$	0.121
8000	$101. \pm 2.1$	$99.4 \pm 0.5$	0.12
14000	$104 \pm 26.$	$108.76 \pm 0.5$	0.1176
30000	$120. \pm 15$	$122.7 \pm 0.5$	0.11
57000	$133 \pm 23$	$135.4 \pm 0.5$	0.11

intercept above 0.5 in the examined energy region.

The obtained value of the total cross sections  $\sigma_{\text{tot}}(s)$  and parameter  $\rho(s, t=0)$  are shown in Table V. At low energies the model calculation of  $\sigma_{\text{tot}}(s)$  corresponds to the experimental data. The inclusion in our fit of the data of the TOTEM Collaboration increases the  $\sigma_{\text{tot}}$  at  $\sqrt{s} = 7$  TeV from 95 mb [24] to 97 mb, which can be compared with recent data [67].

In Table VI, our model calculations at  $\sqrt{s} = 7$  TeV are compared with experimental data obtained at the LHC by different experimental collaborations. On the whole, the model calculations correspond to the existing experimental data. In our opinion, the experimental result of the ATLAS Collaboration  $\sigma_{\text{tot}}(s)$  is preferable.

In Table VII, the comparison of our model with some others are shown. The first is the old Bourrely-Soffer-Wu ( $BSW_1$ ) model [14]. It has a small number of fitting parameters (seven), but it also takes into account the second Reggeon's contributions. We have already noted that in this model the form factor is approximated by some function and it represents the average between the electromagnetic and matter form factors. The recent development of this model is represented as  $BSW_2$  [87]. In this variant the number of experimental points increases, but

TABLE VI: The sizes of the cross sections and the ratio of the  $\sigma_{\text{el}}/\sigma_{\text{inel}}$  at 7 TeV

	$\sigma_{\text{tot}}$	$\sigma_{\text{el}}$	$\sigma_{\text{inel}}$	$R_{\text{el/inel}}$
HEGS <sub>0</sub>	$95.1 \pm 0.8$	$24.1 \pm 0.8$	$65 \pm 0.8$	0.37
HEGS <sub>1</sub>	$97.2 \pm 0.5$	$24.3 \pm 0.5$	$66 \pm 0.5$	0.37
TOTEM	$98.3 \pm 2.9$	$24.8 \pm 1.3$	$73.5 \pm 1.9$	0.34
ATLAS	$95.35 \pm 1.36$	$24.0 \pm 0.6$	$71.34 \pm 0.9$	0.34

TABLE VII: The properties of some models (  $BSW_1$  [14],  $BSW_2$  [87],  $AGN$  [89],  $MN$  [90],  $HEGS_0$  [24],  $HEGS_1$  -present )

	$BSW_1$	$BSW_2$	$AGN$	$MN$	$HEGS_0$	$HEGS_1$
$N_{\text{exp}}$	369	955	1728 + 178	2654 + 238	980	3416
$n_{\text{par}}$	7 + Regge	11 + Regge	35	43	3 + 2	5 + 4
$\sqrt{s}$ , GeV	24 – 630	13.4 – 1800	9.3 – 1800	5 – 1800	52 – 1800	9 – 8000
$\Delta t$ , GeV <sup>2</sup>	0.1 – 2.6	0.1 – 5.	0.1 – 2.6	0.1 – 15	$8.7 \cdot 10^{-4} - 10$	$3.7 \cdot 10^{-4} \div 15$
$(\sum \chi^2)/N$	4.45	1.95	2.46	1.23	1.8	1.28

the number of fitting parameters increases as well. Both of the models (ours and BSW) used the standard eikonal unitarization procedure. Another example of the model (which does not use the unitarization procedure) is based for the most part on Ref. [88]. Its recent variants are presented as AGN[[89]] and MN [[90]]. The work is based on many different forms of the parts of the elastic scattering amplitude with many additional artificial functions. It examined a large number of experimental data points but did not include the Coulomb-hadron interference region. The model includes in the fitting procedure the experimental data of the total cross sections  $\sigma_{\text{tot}}(s)$  and parameter  $\rho(s, t = 0)$ . Such an inclusion decreases the total  $\chi^2$ . Both models summed the statistical and systematic errors and have  $\chi^2/N$  2.46 and 1.23, respectively. The obtained  $\chi^2$  is minimal in the model MN but with a huge

number of fitting parameters and the inclusion of additional artificial functions. Only our model takes into account the whole region of momentum transfer ( $3.75 \cdot 10^{-4} \geq |t| \geq 15 \text{ GeV}^2$ , which includes the high-precision experimental data in the Coulomb-hadron interference region.

A small number of fitting parameters will make it possible to explore some fine additional effects like possible oscillations of the scattering amplitude and find some corrections to the standard eikonal unitarization procedure.

### Acknowledgments

The authors would like to thank J.-R. Cudell and O.V. Teryaev for fruitful discussions of some questions considered in this paper.

- 
- [1] V.A. Matveev, R. M. Muradyan, and A.N. Tavkhelidze, Lett. Nuovo Cimento, **7**, 779 ( 1973).
  - [2] S.J. Brodsky and G.R. Farrar, Phys.Rev.Lett. **31**, 1153 (1973); Lett. Nuovo Cimento, **7**, 779 ( 1973).
  - [3] D.W. Sivers, S.J. Brodsky, and R. Blankenbecler, Phys. Rep. **23**, 1 (1976).
  - [4] M. Jacob and P.V. Landshoff, Mod. Phys. Lett. **A1**, 657, (1986).
  - [5] A.Martin, F. Cheung, *Analytic properties and bounds of the scattering amplitude* (Cordon and Breach, New York, 1970).
  - [6] S.M.Roy, Phys.Rep. **5C**, 125 (1972).
  - [7] R. Fiore, L. Jenkovszky, R. Orava, E. Predazzi, A. Prokudin, and O. Selyugin, Int.J.Mod.Phys. **A24**, 2551 (2009).
  - [8] G. Antchev *et al.* (TOTEM Collaboration), Europhys.Lett. **96**, 21002 (2011).
  - [9] J. R. Cudell and O. V. Selyugin, Czech. J. Phys. **54**, A441 (2004).
  - [10] O. V. Selyugin, J. R. Cudell, and E. Predazzi, Eur. Phys. J. ST **162**, 37 (2008).
  - [11] J. R. Cudell and O. V. Selyugin, Phys. Rev. Lett. **102**, 032003 (2009).
  - [12] T.T. Wu and C.N. Yang Phys.Rev. **175**, 1832 (1968).
  - [13] T.T. Chou and C.N. Yang Phys.Rev. **137**, 708 (1965).
  - [14] C. Bourrely, J. Soffer, and T.T. Wu, Eur.Phys.J. C **28**, 97 (2003).
  - [15] H. Miettinen, Nucl.Phys. **B166** 365 (1980).
  - [16] H. Pagels, Phys.Rev. **144**, 1250 (1966).
  - [17] W. Broniowski and E.-R. Arriola, Phys.Rev. D **78**, 094011 (2008).
  - [18] X.D. Ji, Phys. Lett. **78**, 610 (1997); Phys. Rev D **55**, 7114 (1997).
  - [19] A.V. Radyushkin, Phys. Rev. D **56**, 5524 (1997) .
  - [20] S. Sanielevici and P.Valin, Phys.Rev. D **29**, 52 (1984).
  - [21] J. R. Cudell, E. Martynov, O. V. Selyugin and A. Lengyel, Phys. Lett. B **587**, 78 (2004).
  - [22] A. Donnachie and P.V. Landshoff, Phys. Lett., B **727**, 500 (2013).
  - [23] G. Latino *et al.* (TOTEM Collaboration), arXiv: 1110.1008.
  - [24] O.V. Selyugin, Eur.Phys.J. C **72**, 2073 (2012).
  - [25] O. V. Selyugin, Nucl.Phys. **A 903** 54 (2013).
  - [26] A. Donnachie and P.V. Landshoff, arXiv:1309.1292
  - [27] O.V. Selyugin, Mod. Phys. Lett. **A9**, 1207 (1994).
  - [28] O.V. Selyugin, Mod. Phys. Lett. **A14**, 223 (1999).
  - [29] O. V. Selyugin, Phys. Rev. D **60**, 074028 (1999).
  - [30] O.V. Selyugin, Physics of Particles & Nuclei, **45** 37 (2014).



- [31] O.V. Selyugin and O.V. Teryaev, Phys.Rev. D **79** 033003 (2009).
- [32] M. Guidal, M.V. Polyakov, A.V. Radyushkin, and M. Vanderhaeghen, Phys. Rev. D **72** , 054013 (2005)
- [33] A.D. Martin, R.G. Roberts, W.J. Stirling, and R.S. Thorne, Phys. Lett. B **531**, 216 (2002).
- [34] Spires Durham database, <http://durpdg.dur.ac.uk/hepdata>.
- [35] O.V. Selyugin, Phys. Rev. D **89**, 093007 (2014) .
- [36] M. Diehl, T. Feldmann, R. Jakob, and P. Kroll, Eur.Phys.J. C **39**, 1 (2005).
- [37] L. Andivahis *et al.*, Phys.Rev. D **50**, 5491 (1994).
- [38] J. Arrington, W. Melnitchouk, and J.A. Tjon, Phys.Rev. C **76**, 035205 (2007).
- [39] R.C. Walker *et al.*, Phys.Rev. D **49**, 5671 (1994).
- [40] W. Bartel Nucl.Phys. **B58**, 429 (1973).
- [41] A.F. Sill *et al.*, Phys.Rev. D **48**, 29 (1993).
- [42] P.E. Bosted *et al.*, Phys.Rev.Lett. **68**, 3841 (1992).
- [43] X. Zhan *et al.*, Phys.Lett. B **705**, 59 (2011).
- [44] G. Ron *et al.*, Phys.Rev., **C84**, 055204 (2011).
- [45] C.B. Grawford *et al.*, Phys.Rev.Lett. **98** , 052301 (2007).
- [46] F. Borkowski, *et al.*, Nucl.Phys. **B93**, 461 (1975).
- [47] B.D. Milbrath, *et al.*, Phys.Rev.Lett. **80**, 452(1998); Phys.Rev.Lett. **82**, 2221(E) (1999).
- [48] M.K. Jones *et al.*, Phys.Rev. C **74**, 035201 (2006).
- [49] O. Gayou *et al.*, Phys.Rev.Lett. **88**, 092301 (2002).
- [50] G. Kubon *et al.*, Phys.Lett. B **524**, 26 (2002).
- [51] J. Bermuth *et al.*, Phys.Lett. B **564**, 199 (2003).
- [52] D.I. Glazier *et al.*, Eur.Phys.J. A **24**, 101 (2005).
- [53] S. Riordan *et al.*, Phys.Rev.Lett. **105**, 262302 (2010).
- [54] R. Madey *et al.*, Phys.Rev.Lett. **91** 122002 (2003).
- [55] S. Rock, Phys.Rev.Lett. **49**, 1139 (1982).
- [56] W.K. Brooks and J.D. Lanchiet, Nucl.Phys. **A755**, 261 (2005).
- [57] J. Lanchiet *et al.*, Phys.Rev.Lett. **102**, 192001 (2009).
- [58] P. Markowitz *et al.*, Phys.Rev. C **48**, R5 (1993).
- [59] E.E.W. Bruins *et al.*, Phys.Rev.Lett. **75**, 21 (1995).
- [60] T. Eden *et al.*, Phys.Rev. C **50**, 1749 (1994). , R. Madey, W.M. Zhang, B.D. Anderson, H. Arenhovel, A.R. Baldwin, D. Barkhuff, K.B. Beard, W. Bertozzi, J.M. Cameron *et al.*,
- [61] J. Becker *et al.*, Eur.Phys.J. A **6**, 329 1999.
- [62] H. Zhu *et al.*, Phys.Rev.Lett. **87**, 081801 (2001).
- [63] G. Warren *et al.*, Phys.Rev.Lett. **92**, 042301 (2004).
- [64] D. Rohe *et al.*, Phys.Rev.Lett. **83**, 4257 (1999).
- [65] S. Alekhin, J. Blumlein, S. Klein, and S. Moch, Phys.Rev. D **81**, 014032 (2010);
- [66] S. Alekhin, J. Blumlein, and S. Moch, Phys.Rev. D **86** , 054009 (2012).
- [67] G. Antchev *et al.* (TOTEM Collaboration), arXiv:1503.08111.
- [68] U.Amaldi and K.R. Schubert, Nucl.Phys. **B166**, 301 (1980).
- [69] A. Degasperis and E. Predazzi, Nuovo Cimento **A65**, 764 (1970).
- [70] R. Fiore, L.L. Jenkovszky, and F. Paccanoni, Phys. Rev. D **54**, 6651 (1996).
- [71] A. Anselm and V. Gribov, Phys. Lett. **B40**, 487 (1972).
- [72] V.A. Khoze, A.D. Martin and M.G. Ryskin, J.Phys.G **42**, 025003 (2015).
- [73] M.V. Galynskii and E.A. Kuraev, JETP Lett. **96**, 6 (2012).
- [74] I. Sitnik, Comput.Phys.Comm. **185**, 599 (2014).
- [75] A.D. Martin, W.J. Stirling, R.S. Thorne, and G. Watt, Eur.Phys.J. C **63**, 189 (2009).
- [76] G. Watt, Nucl.Phys. B, Proc.Suppl. **222-224**, 61 (2012).
- [77] G. Antchev *et all.* (TOTEM Collaboration), Europhys.Lett. **95**, 41001 (2011).
- [78] ATLAS Collaboration, Nucl.Phys. **B889**, 486 (2014).
- [79] A.A. Kuznetsov *et all.*, Sov.J.Nucl.Phys. **33**, 74 (1981)( Yad.Fiz. **33**, 142 (1981).
- [80] O. Selyugin, Phys. Lett. B **333**, 245 (1994)
- [81] O.V. Selyugin, Nucl.Phys. **A922**, 180 (2014).
- [82] S.V. Goloskokov, S.P. Kuleshov, and O.V. Selyugin, Sov.J.Nucl.Phys. **46**, 120 (1987)
- [83] J. Beringer *et all.* (Particle Data Group), Phys. Rev. D **86**, 010001 (2012).
- [84] M.M. Block and R.N. Cahn, Rev.Mod.Phys. **57**, 563 (1985).
- [85] J.-R. Cudell, E. Predazzi, O. V. Selyugin, Phys.Rev. D **79** , 034033 (2009).
- [86] O. V. Selyugin and J.-R. Cudell, AIP Conf.Proc. **1350**, 115 (2011).
- [87] C. Bourrely, Eur.Phys.J. C **74**, 2736 (2014).
- [88] P. Gauron, E. Leader, and B. Nicolescu, Phys. Lett. **B238**, 406 (1990).
- [89] R. Avila, P. Gauron, and B. Nicolescu, Eur. Phys.J. **C49**, 581 (2007).
- [90] E. Martynov and B. Nicolescu, Eur. Phys. J. C **56**, 57 (2008).